eprints@whiterose.ac.uk
https://eprints.whiterose.ac.uk/

Dust Devil Dynamics

W. Horton,[1,2] H. Miura,[3] O. Onishchenko,[4,5] L. Couedel,[2] C. Arnas,[2] A.

Escarguel,[2] S. Benkadda,[2] V. Fedun[6]

————

[1]The University of Texas at Austin, USA.

[2]Laboratorie de Physique des Interactions

Ioniques et Moleculaires, Centre National de

la Recherche Scientifique/Aix–Marseilles

Universities, 13397 Marseilles, France.

[3]National Institute for Fusion Science,

509–5292 Toki, Japan.

[4]Institute of Physics of the Earth, 10 B.

Gruzinskaya, 123242 Moscow, Russian

Federation.

[5]Space Research Institute, 84/32

Profsoyuznaya str., 117997 Moscow,

Russian Federation.

[6]University of Sheffield, Mappin Street

Sheffield, S1 3JD United Kingdom.

Abstract.

A self–consistent hydrodynamic model for the solar heating driven onset of a dust devil vortex is derived and analyzed. The toroidal flows and vertical velocity fields are driven by an instability that arises from the inversion of the mass density stratification produced by solar heating of the sandy surface soil. The nonlinear dynamics in the primary temperature gradient driven vertical air flows drives a secondary toroidal vortex flow through a parametric interaction in the nonlinear structures. While an external tangential shear flow may initiate energy transfer to the toroidal vortex flow, the nonlinear interactions dominate the transfer of vertical–radial flows into a fast toroidal flow. This secondary flow has a vertical vorticity while the primary thermal gradient driven–flow produces the toroidal vorticity. Simulations for the complex nonlinear structure are carried out with the passive convection of sand as test particles. Triboelectric charging modeling of the dust is used to estimate the charging of the sand particles. Parameters for a Dust Devil laboratory experiment are proposed considering various working gases and dust particle parameters. The nonlinear dynamics of the toroidal flow driven by the temperature gradient is of generic interest for both neutral gases and plasmas.

_____

Key Points.

∘ Main point #1: Surface heating drives unstable gravity waves that develop into complex dust devil vortices.

∘ Main point #2: Toroidal rotation in dust devils evolves form the driven vertical flows from the surface layer producing complex 3D structures.

∘ Main point #3: Validation with laboratory experiments of the complex theory-simulation model of the dust devil will improve weather predictions.

1. Introduction

Dust devils are localized, complex vortical structures driven by inverted temperature gradients over hot, dry sandy soils and give one of the possible mass flow configurations inferred from the dust devil field data taken from *Balme and Greeley* [2006]. Figure 1(a)-(b) show the structure given by Balme and Greeley. Figure 2 gives our version of the electrical structure from the differential motion of the dust, aerosol, particles from the triboelectric charging of the sand transported by the hydrodynamic flows reported in the field observations along with knowledge from plasma physics of toroidal structures. In the lower core of the structure the atmospheric flow patterns are of rising hot air. Outside the core there is falling of cooled air. From the field data there is also the tangential, and thus a toroidal flow velocity v_θ shown in Fig. 2. The toroidal flow adds to the vertical flow to produce the swirling helical structures of dust devils.

The vortex structure moves horizontally so as to feed on new layers of inverted mass density material, thus maintaining the power driving the kinetic energy of the vortex against friction and viscosity. While external horizontal wind shear may enhance the strength of the vortex, external sheared flow is not an essential ingredient in our analysis, owing to the nonlinear transfer of energy from the poloidal to the toroidal flows.

The solar heating of the surface layer of air at atmospheric pressure creates convectively unstable layer with the temperature gradient larger than the adiabatic gradient. The pressure gradient term contains the buoyancy forces and gives the eigenmodes for the Brunt–Väisälä frequency of the vertical/horizontal convection. The condition when the square of the Brunt–Väisälä frequency is negative corresponds to the Schwarzschild crite-

rion [*Schwarzschild*, 1998] for atmosphere instability against convection. The dynamical rate of growth is estimated from $(g/L_p)^{1/2}$ where the mass density scale length L_p is much less than the pressure gradient scale height H in the hot desert atmosphere. For incompressible motions in a gas with adiabatic gas constant γ the formula for the Brunt–Väisälä frequency becomes $(gd\ln\theta/dz)^{1/2}$ where θ is the potential temperature for the gas. The unstable air dynamics drives an upward and horizontal air flow from the energy released by gravity from the reversed mass density in the hot–surface air layer. The instability follows simply from the formulas for internal gravity waves with the equation of state for air. The critical vertical–temperature gradient for the onset of the dust devil vortex is derived and approximated as observed of 1-10º C/m, in the first few meters of hot surface air over the sandy soil.

As the critical temperature gradient is reached, the low–frequency $f <$ mHz internal gravity waves become [bifurcate] complex exponential growing modes. These unstable gravity waves produce vertical–horizontal vortex flow structures rising from $100\,\mathrm{m}$ to $1\,\mathrm{km}$ with their vorticity vector $\omega = \nabla \times v$ in the horizontal plane. Without external sheared–horizontal winds the flow becomes unstable through a nonlinear bifurcation to a horizontal toroidal flow that can exceed the velocities of the original vertical–horizontal flow. The higher–speed toroidal or tangential flow creates a lower–pressure region in the core of the dust devil structure that has been measured in several field experiments and modeled in several computer simulations [*Houser, et al.*, 2003].

The dust is pulled up in the core by the frictional drag on the air and the electrostatic repulsion owing to electric charge differences between the smaller and large diameter dust particles from the triboelectric effect. The vertical/horizontal flow has a toroidal vorticity

which either lifts the dust and sand directly or balances the downward gravitational force on the sand sufficiently to allow electrostatic forces from triboelectricity to lift the smaller, lighter sand and dust into a high rising column [*Kok and Renno*, 2006]. The bouncing of the sand, called saltation, transfers weakly–bound surface electrons from the larger to the smaller diameter particles (sand – principally SiO_2 during the collisions [*Lacks and Levandowsky*, 2007]. Each grain forms a small capacitor with capacitance given by $C_d = 2\pi\epsilon_0 d$ where d is the diameter of the grain and ϵ_0 is the free space permeability. The vertical stratification of the grains by mass separates the particles so that the lighter negatively–charged particles rise to the top of the vortex structure as shown in *Balme and Greeley* [2006]. The result is a large vertical electric field and a large electric dipole moment shown as $\boldsymbol{P}$. The first observations [*Freier*, 1960; *Crozier*, 1970] on dust devils report measuring a kV/m vertical electric field and give estimates of the electric dipole moment $\boldsymbol{P}_E$ of order a Coulomb–meter red[C-m] from the first data on dust devils. This electric field then enhances the pickup, or lifting, of the smaller sand grains as shown in the experiments of *Kok and Renno* [2006]. Thus there is feedback loop in the charge separation that builds up the electric dipole moment and the lifts the negatively–charged grains of sand to considerable heights $H > 100\,\text{m}$. Since the vortex structure is dynamical with significant fluctuations, the oscillations of the charged dust generates radio frequency (RF) waves from the oscillations of the charges as well as an acoustical signal that is heard and recorded in movies of dust devils. In addition, the circular vortex motion of the charges creates a fluctuating magnetic field.

Houser, et al. [2003], with data taken in July 2000, outside Boulder City, Nevada, gave typical dust devils with $2R_0 \sim 10\,\text{m}$ diameter and $H \sim 100\,\text{m}$ height. The electromagnetic

emission was recorded at two bands: 5-20 Hz and 30-50 Hz. The peak emission is steady for 10 s and decreases over the next 25 s as shown in magnetic spectrograms in *Farrell, et al.* [2000]. In June 2001 a campaign was carried out in Arizona 5 km southwest of Eloy, Arizona with scientists from GSFC, UC Berkeley, Glenn RC, Ames, JP:L and Optech, Inc. This campaign used a variety of instruments simultaneously integrating the data at high speed of 40 kS/s. Studies of the individual events are found in *Renno, et al.* [1998] and a summary of the MATADOR 2002 field test is given in *Renno, et al.* [2004]. Since that early study the nature of the wind–driven pickup of the grains by triboelectric charging has been parameterized in more detail by several research groups [*Lacks and Levandowsky, 2007*].

Kok and Renno [2006] observe that mineral dust aerosols have a strong effect on the Earth's climate by absorbing and scattering solar radiation. The dust also serves as a seed for the formation of condensation of ice nuclei [*Twomey, 1974; DeMott, et al., 2003; Kok and Renno, 2006*]. The current limited understanding of the level of dust in the atmosphere leads to large uncertainties in prediction of global climate changes [*Intergovernmental Panel on Climate Change, 2001, 2007*]. Owing to their micron to hundred nanometer size, mineral dust aerosol interactions have relatively large interparticle forces when compared with forces from the wind stress forces. These interparticle forces inhibit the dust aerosols from being directly lifted by surface winds. As noted above, the smaller charges are charged negatively and the larger particles charged positively owing to differences in the surface quantum states. *Lacks and Levandowsky* [2007] test formulas for the probability distributions for dependence of the charges versus the radius of the particles in molecular dynamics simulations. Saltation is the process by which the sand and dust particles are

moved by the wind, bouncing along the surface against the force of gravity. The collisions between the larger and smaller bouncing particles gives the smaller particles a negative charge. There is a complex interplay between gravity, electric forces and wind shear stress that ejects, or lifts, the dust into the air. Once the small mineral particles are ejected they are transported by the frictional force from the wind and vortex flows for long distances and to high altitudes. *Kok and Renno* [2006] report laboratory data on the critical electric field required to lift sand grain particles of several sizes. They report experiments with Sonoran desert particles in Arizona ranging from 20 to 300μ m with fourteen sample sizes to test the formulas derived for the lifting conditions. The experiments show the critical electric field above which the particles are lifted. The authors give a formula for the wind velocity threshold combined with the electric field threshold for lifting sand particles.

Noting that dust grains with a large–to–small radius ratio of five have a ratio of the electrical capacitance of 5. Then elastic collisions of ensembles of particles show that the loosely bound surface electrons on the larger dust grains are transferred to the smaller diameter dust grains. The complex solid state physics of the process is described by triboelectric theory. Molecular dynamics simulations for ensembles of dust grains with these rules applied on each collision show that the smaller diameter particles trap more electrons transferred from the larger diameter dust grains. After 10^5 collisions [*Lacks and Levandowsky*, 2007] show that bimodal charge distributions develop with the smaller diameter dust have a negative charge and the large dust grains having a positive charge. The rules for the charge transfer involve the equalization with Fermi level electron states during the period of contact in the collision with loosely bound electrons in surface effect energy states.

One of the earliest reports estimating the electric field is *Freier* [1960] from dust devils observed in the Sahara Desert, West Africa at the time, during the a solar eclipse expedition. The report notes the field reaches at least $400\,\mathrm{V/m}$ and could be modeled by an electric dipole moment $M = 0.6\,\mathrm{Cm}$ (reported as $1.7 \times 10^9\,\mathrm{esu\,m}$ at the height of $h = 21.4\,\mathrm{m}$ with a speed of $4\,\mathrm{m/s}$). During September the frequency of large dust devils was about one per day. The electric field was measured with an electric field mill. A report by *Crozier* [1970] on *Dust Devil Properties* gives a table of data for $17\,\mathrm{DDs}$ in New Mexico; total charges estimated from $0.001\,\mathrm{C}$ to $0.05\,\mathrm{C}$ and charge densities ranging from 1.0×10^{11} to 9×10^{17} electrons/m^3. The electric dipole moments reported ranged from 0.01 to $5\,\mathrm{C}$-m. For one of the middle–sized DD the electric field estimate is given as 1.0×10^{11} to 9×10^{17} as $1.5\,\mathrm{V/m}$ but the report notes that $3\,\mathrm{kV/m}$ would exceed the range of the instrument. The report states the dust devils are negatively charged. The observer notes that the shape of the dust devil changes on a minute time scale. *Balme and Greeley* [2006] carried out a series of laboratory experiments to identify key parameters and their values. Balme scans over diameters of 100, 200 and $300\mu\,\mathrm{m}$ with ensembles of 20,000 test particles injecting the particles in a $50\,\mathrm{m}$ area around the core of the vortex at the rate of 400 particles per second for 5 seconds. This is equivalent to an injection rate of $10\,\mathrm{kg/s}$ or comparable to that reported in *Renno, et al.* [1998]. The lighter particles stay near the core and the heavier ones move with helical orbits around the core migrating to the edge. This is understood in terms of the difference in the centrifugal force acting on the particles. While the basic reference particle is quartz for the sand particles of the desert soils, one notes that dust devils also occur in areas with some vegetation [*Oke, et al.*, 2007] and some simulations were carried out with wood density particles [*Greeley, et*

al. (2005)]. There are observations by Mars explorers of giant dust devils adding further to the interest in the complex dynamics [*Farrell, et al.*, 2004]. A curious event is noted on the NASA website of the change in the performance of a solar panel array after the passage of Martian dust devil over the panel. There are many large tracks over the surface of Mars from the dust devils.

The topology of the combined horizontal circular motion and up–down vertical motion of the neutral atmosphere and the charged sand/dust particles makes the phenomenon of interest to plasma physics, triboelectricity and to hydrodynamics. The axisymmetric toroidal plasma physics confinement experiments exhibit a coupling between the driven poloidal flow and a spontaneously–generated toroidal rotation [*Horton*, 2012]. In addition, the plasma physics interest in dust devils arises from the rapid transport of the frictional triboelectric charging of the micron–sized molecular dust grains that are analogous to charging of molecular clumps of material from the surface of the vessel containing the hot fusion plasma. The core plasma is at temperatures greater than the core of the sun $[10\,\mathrm{KeV} \sim 10^8\,\mathrm{K}]$ and the coated walls are a few meters away from the core. While there are important differences in the microscopic physics, the polarization of the charged grains is a common feature and the associated electric forces on the dust grains are important in the transport modeling. The plasma physics interest in dust devils arises also from the similarities between the electrodynamics of the charged particles in dust devils and the dynamics in dusty (complex) laboratory plasmas even though the charging mechanisms are different: triboelectric charging in the case of dust and collisions between electrons and molecules in the second case. Secondly, large vortex structures, i.e. 'Solar Tornado'

are commonly observed convectively–driven regions of the solar atmosphere [*Wedemeyer, et al.* [2012] and *Li, et al.* [2012].

We use simple parameterizations from the Lacks and Levandowsky [2007] experiments in our hydrodynamic model to calculate the amount of sand and mineral dust raised in a dust devil. The explicit of the hydrodynamics may add confidence in the meteorology communities' ability to estimate and forecast the amount of material in the atmosphere to be used in global circulation models of the troposphere. From the particle charge distribution versus particle radius distribution shown in *Lacks and Levandowsky* [2007], we can estimate the vertical electric field from the stratification of the particles. As an example, we note that the dust storms in the Panhandle in northwest Texas bring significant layers of dust into homes in Austin and San Antonio, more than $500\,\mathrm{km}$ southeast. The dust storms can reduce visibility to $1\,\mathrm{km}$ [*Goudie*, 1983].

In Sec. 2(a) the generation of the dust devil by the unstable vertical convection is derived in the vertical/horizontal flow velocities which is driven by the vertical temperature gradient. In Sec. 2(b) the nonlinear coupling of the toroidal vorticity to a vertical vorticity is derived. The energy conservation and the flow of the cross–helicity equations are analyzed. In Sec. 3.2 the numerical simulations are discussed and the transport of the dust is calculated. Sections 3 and 4 discuss the desert observational data and the proposed laboratory experiment required to validate the theory-simulation model for weather forecasting. Section 5 gives the conclusions.

2. Dust Devil Generation from Temperature Gradients

A self–consistent hydrodynamic model for the generation of a dust devil vortex arises naturally from the unstably stratified atmosphere as do other cyclonic/anticyclonic struc-

tures. The poloidal flows [horizontal/vertical v_r, v_z flows] are driven by the instability that arises from the inversion of the mass density stratification (a form of the Rayleigh–Taylor instability) from solar heating of the air by the hot sandy surface soil. We show that the initial unstable vertically stratified atmosphere results in large–scale toroidal motion generating the dust devil vortex structures. The velocities are low compared with the speed of sound 300 m/s and thus we take them as incompressible as given by the stream function $\Psi(r, z)$ where $v_r = -(\partial \Psi / \partial z)$ and $v_z = (\partial \Psi / \partial r)$.

The formation of dust devils is associated with an intrinsic atmospheric instability driven by the solar heating. The relatively low diffusive heat transfer and absorption of thermal radiation emitted by the ground produces the temperature stratification with cooler, denser gas over the warmer, less dense gas that naturally unstable. The instability manifests itself as convective plumes and vortices as shown in Sec. 3 with 3D simulations. The dust devil is a visible manifestation of a vortex that has lifted dust and sand directly from the surface. In these vortices, warmer air from the ground travels upward in the central region, and cooler air is pulled downward both within the core and the outer regions surrounding the vortex. Dust entrained in the upward moving fluid elements gives rise to the opaque central region. *Renno, et al.* [1998] describes the process in a Lagrangian sense, with cooler air down–drafted in the outer regions to merge with the ground heated fluid elements that are drawn inward to the dust devil center. Then heated elements propagate upward again in the central region, thus forming a heat engine with the ground as the primary energy source. This mechanism has also been proposed to explain water spouts [*Renno and Bluestein*, 2001].

2.1. Two– and three–dimensional dust devil dynamics

In the gravitational, unstable lower level of the air, there are two types of nonlinear vortices. They are 2D rolls and three–dimensional vortex rings. For the two–dimensional rolls we take axis of the roll in the y–direction which wraps in to ring becoming the azimuthal direction ϕ in the vortex ring in the 3D vortex. The vertically–upward fluid motion with velocity v_z and the horizontal motion with velocity v_x. For 2D incompressible flow the velocity in a vertical slice across the vorticity vector is called the poloidal plane. In this plane the velocity vector is derived from the stream function Ψ as follows:

$$v = \hat{y} \times \nabla\Psi = \left(\frac{\partial\Psi}{\partial z}, 0, -\frac{\partial\Psi}{\partial x}\right) = (u, v, w). \tag{1}$$

The curl (rotation) of momentum equation gives

$$\frac{\partial}{\partial z}\rho\frac{\partial}{\partial z}\frac{\partial}{\partial t}\Psi + \frac{\partial}{\partial x}\rho\frac{\partial}{\partial x}\frac{\partial}{\partial t}\Psi = g\frac{\partial}{\partial x}\rho. \tag{2}$$

The conservation of mass for the incompressible 2D flow is

$$\frac{\partial\rho}{\partial t} - \frac{\partial\Psi}{\partial x}\frac{\partial\rho}{\partial z} + \frac{\partial\Psi}{\partial z}\frac{\partial\rho}{\partial x} = 0. \tag{3}$$

The amplitude of the waves increases with height as the density drops from the conservation of energy.

In the 3D vortex flow we use $u = v_r$ and $w = v_z$ for the velocity flow in the poloidal plane and v_ϕ is the toroidal velocity. Here (r, ϕ, z) are the cylindrical coordinates. We will assume the mean fields averaged over the fluctuations have symmetry in the toroidal angle variable ϕ. The conservation equation for the airborne dust of mass density ρ_d, along with the surface layer source term S_d, is given by

$$\frac{\partial\rho_d}{\partial t} + \frac{1}{r}\left[\frac{\partial\rho_d}{\partial r}\frac{\partial\psi}{\partial z} - \frac{\partial\rho_d}{\partial z}\frac{\partial\psi}{\partial r}\right] = S_d w(z_m, x, t), \tag{4}$$

where there is a source of dust proportional to the upward air velocity near the surface at z_m. Equation (4) is in the limit of vanishing slippage between the dust and air flow in a small–surface layer at $z = z_m$. The source of the dust at the layer z_m is defined where $dw/dz = 0$ or w is a maximum and then S_d is the surface density at the top of the boundary layer of the bouncing/saltating dust, as described in Fig. 2.

In the approximation where the density under the operators on the left–hand side of Eq. (3) can be taken as constant the operator on ψ is the Grad–Shafranov operator of equilibrium toroidal MHD. The operator is denoted by Δ^* in plasma physics and numerous programs are available for inverting the Grad–Shafranov problem. The linearized forms of the density–weighted toroidal–vorticity equation determines the eigenmodes of the convection. For the vertical mass density function $\rho(z)$ the Laplace transform of $\exp(\gamma t)$ of the toroidal vorticity equation gives

$$r\frac{\partial}{\partial r}\frac{\rho}{r}\frac{\partial}{\partial r}\Psi + \frac{\partial}{\partial z}\rho(z)\frac{\partial}{\partial z}\Psi = \frac{\rho N^2(z)}{-\gamma^2}r\frac{\partial}{\partial r}\frac{1}{r}\frac{\partial}{\partial r}\Psi. \tag{5}$$

In Eq. (5) the function $N^2(z)$ is the Brunt–Väisälä frequency from the vertically mass density profile $\rho(z)$.

In the limit of weak stratification above the unstable mixing layer, we can reduce the full nonlinear dynamics as incompressible 3D turbulence with

$$\begin{aligned}
\omega &= \nabla \times v, \\
\frac{\partial \omega}{\partial t} + v \cdot \nabla \omega &= \omega \cdot \nabla v + \nabla \rho \times \frac{\nabla p}{\rho^2}
\end{aligned} \tag{6}$$

where ω is vorticity and gravity is implicit in the mass density stratification ρ. There is now a Poisson equation to solve to the pressure distribution which will have a lower–pressure core in the dust devil to balance the centrifugal force from the higher rotational velocity. The pressure drop in the core is measured in the field data. The pressure profile

follows by solving the Bernoulli equation

$$\Delta\left(\frac{p}{\rho} + \frac{1}{2}v^2\right) = -\nabla \cdot (v \times \omega). \tag{7}$$

Once the convection has reached a steady state, a simple, classical vortex solution of the axisymmetric 3D Navier–Stokes equations – without the vertical stratification – applies. The steady state solution is the Burgers vortex. (Burgers vortex is an exact solution to the Navier–Stokes equations governing viscous flow.) We apply this solution and use it to assess the pressure field from the computer simulations of incompressible vortex flow. The Burgers vortex gives the pressure drop from the high speed flows in the core of the dust devil that are an expression of the Bernoulli law. The Bernoulli law in the vortex flow states that the cross–product of the vorticity and flow velocity vectors give rise to a force balancing the gradient of the dynamical pressure that is the sum of the thermal pressure per unit mass and the kinetic pressure from flow velocity. The cross product of the vorticity vector and the flow velocity are analogous in plasma physics vortex problem to the $\mathbf{j} \times \mathbf{B}$ force where the incompressible velocity field plays the role of the magnetic field and the vorticity is the current density $\mathbf{j}$.

The core of the vortex is a viscous region where the flow is converted from radially–converging to upward–increasing velocity. The flow in this core region is close to that given by the Burgers vortex with stream function $\Psi(x,z) = \omega_z = \alpha r^2 z/2$, which gives the flow fields

$$\begin{aligned} v_r &= -\alpha r/2 \\ v_z &= \alpha z \\ v_\phi &= u_\phi(r). \end{aligned} \tag{8}$$

The toroidal flow velocity v_ϕ is determined by the radial force balance equation and the equation for the axial vorticity ω_z with viscosity ν. The toroidal velocity is given as

$$u_\theta = \frac{\alpha\Gamma}{2\pi\nu}\left(1 - \exp\left(-\frac{\alpha r^2}{4\nu}\right)\right).$$ (9)

Returning to the radial force balance equation and calculating the radial integral of the centrifugal acceleration, one obtains the depression in the pressure field given by

$$\frac{p}{\rho} = \frac{p_o}{\rho_o} - \frac{1}{2}\alpha^2 z^2 - \frac{1}{8}\alpha^2 r^2 - \left(\frac{\alpha\Gamma}{2\pi r}\right)^2 \int_r^\infty dr_1 r_1^{-3}\left[1 - e^{-\alpha(r_1)^2/4\nu}\right]^2.$$ (10)

In this vortex [*Kida and* , 1998] the pressure drops in the core of the dust devil by

$$\frac{p - p_o}{\rho_o} \simeq -\frac{(\alpha\Gamma/2\pi)^2}{2r^2} \text{ for } r \geq 2.24\left(\frac{\nu}{\alpha}\right)^{1/2}.$$ (11)

Measured pressure drops in the core of the dust devils are of order $100\,\mathrm{Pa}$ [*Balme and Greeley*, 2006]. The pressure drops to a local minimum at $r_{\min}$ given approximately by

$$r_{\min} = 2\left(\frac{\Gamma}{2\pi}\right)^{\frac{1}{2}}\left(\frac{\nu}{r_d^2\alpha}\right)^{1/3}.$$ (12)

The exponential growth of the vertical vorticity from the nonlinear interactions between the poloidal and toroidal velocities in the nonlinear dynamics is derived following the analysis of *Onishchenko, et al.* [2014].

2.2. Axisymmetric solutions of the 3D dust devil flows

In the current study of the waves in the atmosphere we neglect the influence of dissipative processes, i.e. viscosity, thermal conductivity, heat flow from outside, friction, etc. The initial set of equations is the equation of motion (18) and (14) and the transport equation (19) for the potential temperature $\theta = p^{1/\gamma}/\rho$:

$$\frac{d\mathbf{v}}{dt} = -\frac{1}{\rho}\nabla p + \mathbf{g},$$ (13)

and

$$\frac{d\theta}{dt} = 0. \tag{14}$$

Here ρ and p are the density and pressure respectively, $d/dt = \partial/\partial t + \mathbf{v}\nabla$ is the Euler (convective) time derivative, $\mathbf{v}$ is the velocity of matter, $\mathbf{g} = -g\hat{\mathbf{z}}$ is the gravity acceleration and $\hat{\mathbf{z}}$ is the unit vector directed along the vertical axis z. We use the ideal gas law $p/\rho T = \text{const}$, where T is the temperature to complete the set of equations .

In terms of the vorticity vector, $\omega = \nabla \times \mathbf{v}$, the dynamics reduces to

$$\frac{\partial\omega}{\partial t} + (\mathbf{v}\cdot\nabla)\omega = (\omega\cdot\nabla)\mathbf{v} + \frac{1}{\rho^2}[\nabla\rho\times\nabla p]. \tag{15}$$

As a result, from Eqs. (13) and (14) one obtains a system of two nonlinearly coupled equations for the poloidal stream function ψ and the normalized mass density fluctuation $\chi = g\tilde{\rho}/\rho_0$ combine to give

$$\frac{\partial}{\partial t}\left(\Delta^*\psi + \frac{d\ln(\rho_0)}{dz}\frac{d\psi}{dz}\right) + \frac{1}{r}J\left(\psi,\Delta^*\psi\right)$$

$$= -r\frac{\partial\chi}{\partial r} + \frac{r}{\rho_0^2}J(\tilde{\rho},\tilde{p}) \tag{16}$$

coupled to

$$r\frac{\partial\chi}{\partial t} - \omega_g^2\frac{\partial\psi}{\partial r} + \{\psi,\chi\} = 0 \tag{17}$$

where

$$\Delta^* = r\frac{\partial}{\partial r}\frac{1}{r}\frac{\partial}{\partial r} + \frac{\partial^2}{\partial z^2}, \tag{18}$$

In obtaining Eq. (17) we neglect by the wave–pressure perturbations compared to the density perturbations, considering low–frequency waves when $(\omega^2/c_s^2 k_r^2)L_\rho\partial/\partial z \ll 1$, where ω and k_r are the characteristic wave frequency and respective wavenumber,

$L_\rho^{-1} = d(\ln\rho)/dz$ is the characteristic density inhomogeneity scale in vertical direction. Beforehand, we consider that $|v_z| \gg |v_r|$, i.e. consider that $\partial/\partial r \gg \partial/\partial z$.

In the linear approximation one derives the growth of the vertical vorticity from initial poloidal flows. From equations (16) and (17) one finds that

$$\frac{\partial^2}{\partial t^2}\left(\Delta^*\psi - \frac{\psi}{4L_\rho^2}\right) = -\omega_g^2\left(r\frac{\partial}{\partial r}\frac{1}{r}\frac{\partial}{\partial r}\right)\psi. \tag{19}$$

In the unstably–stratified layer ($\omega_g^2 < 0$) and in the approximation $\partial/\partial r \gg 1/L_\rho$, we obtain from Eq. (19) $\psi \propto \exp(\gamma t)$ where $\gamma = |\omega_g|$.

2.3. Exponential Growth of the Toroidal Rotation

Consider a simplified model for the stream function

$$\psi = \frac{\alpha r^2 z}{2} \cdot \exp\left(\gamma t - \frac{r^2}{r_0^2}\right), \tag{20}$$

where r_0 is the vortex radius. Then $\Delta^*\psi = -4\alpha\left(2 - \frac{r^2}{r_0^2}\right)\psi$ and

$$v_r = -\frac{1}{r}\frac{\partial\psi}{\partial z} = -\frac{\alpha r}{2}\cdot\exp\left(\gamma t - \frac{r^2}{r_0^2}\right) \tag{21}$$

and

$$v_z = \frac{1}{r}\frac{\partial\psi}{\partial r} = \alpha z\left(1 - \frac{r^2}{r_0^2}\right)\cdot\exp\left(\gamma t - \frac{r^2}{r_0^2}\right). \tag{22}$$

Thus, we have derived exponentially growing ascending flows $v_z > 0$ in the vortex core region at $r < r_0$ and the descending flow $v_z < 0$ in the external region at $r > r_0$. The computer simulations in Sec. 3 of the full hydrodynamics are consistent with this analytic result but show the flows can be pulsating in time.

$$\omega_\phi = \frac{\partial v_r}{\partial z} - \frac{\partial v_z}{\partial r} = \frac{1}{r}\Delta^*\psi = -\left(\frac{r^2}{r_0^2}\right)\left(2 - \frac{r^2}{r_0^2}\right)\psi. \tag{23}$$

In the linear approximation one obtains from (15) that

$$\frac{\partial \omega_z}{\partial t} + v_r \frac{\partial \omega_z}{\partial r} = \omega_z \frac{\partial v_z}{\partial z}. \tag{24}$$

Thus the parameter α corresponds to the horizontal vorticity at $2rz = r_s^2$, where r_s^2 is the radius at $t = 0$. To derive the evolution of the vertical vorticity ω_z we use

$$\frac{\partial \omega_z}{\partial t} + v_r \frac{\partial \omega_z}{\partial r} = \omega_z \frac{\partial v_z}{\partial z}. \tag{25}$$

For the initial flow $\omega_z = \omega_z(0, r)$ is a large scale seed vorticity. Now we consider the initial state with a small seed initial toroidal rotation given by the vertical vorticity

$$\omega_z(0, r) = \frac{v_0}{R} \left[1 - \exp\left(\frac{-r^2}{R^2}\right) \right] \tag{26}$$

where R is the characteristic radius of the large–scale toroidal component of vorticity ω_z. We consider that $R \gg r_0$. In the approximation $r^2/R^2 \ll 1$ we have $\omega_z(0, r) = \Omega r^2/R^2$. Taking into account (22) we derive an exponential growth of vertical vorticity given approximately by

$$\omega_z(r, t) = \exp\left[\left(\frac{2\alpha}{\gamma}\right) \cdot \exp\left(\gamma t - \frac{r^2}{r_0^2}\right) \right]. \tag{27}$$

Thus, we have established that the kinetic energy released by the inverted mass density stratification is converted into the toroidal flow velocity with exponential growth. The associated growth is described by Eq. (27) of the vertical vorticity. This exponential growth of the vertical vorticity saturates in fully nonlinear dynamics as shown in Sec. 3, when the energy transfer rates come to balance with viscous dissipation and Eckman friction. In the saturated state complex helical structures arise in the saturated nonlinear dynamics.

3. Simulation of the Rotational Spin–up of a Dust Devil

3.1. Outline of the simulations

In this subsection, we solve the compressible Navier–Stokes equations

$$\frac{\partial \rho}{\partial t} = -\frac{\partial (\rho v_j)}{\partial x_j}, \tag{28}$$

$$\frac{\partial (\rho v_i)}{\partial t} = -\frac{\partial (\rho v_i v_j)}{\partial x_j} - \frac{\partial p}{\partial x_i} + \frac{2}{\mathrm{Re}}\frac{\partial}{\partial x_j}\left(S_{ij} - \frac{1}{3}\delta_{ij}\frac{\partial v_k}{\partial x_k}\right) - \rho g \delta_{i,3}, \tag{29}$$

$$\frac{\partial E_T}{\partial t} = -\frac{\partial}{\partial x_j}\left[(E_T + p)\,v_j\right] + \frac{1}{M_0^2 \mathrm{Pr}\ \mathrm{Re}(\Gamma - 1)}\frac{\partial^2 T}{\partial x_j \partial x_j}$$
$$+ \frac{1}{\mathrm{Re}}\frac{\partial}{\partial x_j}\left\{v_i\left[\left(S_{ij} - \frac{1}{3}\delta_{ij}\frac{\partial v_k}{\partial x_k}\right)\right]\right\} - \rho v_3 g, \tag{30}$$

$$E_T = \frac{p}{\Gamma - 1} + \frac{1}{2}\rho v_i v_i, \tag{31}$$

$$p = \frac{1}{\Gamma M_0^2}\rho T, \tag{32}$$

$$S_{ij} = \frac{1}{2}\left(\frac{\partial v_i}{\partial x_j} + \frac{\partial v_j}{\partial x_i}\right) \tag{33}$$

for the dust devil dynamics. These equations have been normalized by the reference length L_0, the velocity V_0, the mass density ρ_0, obtaining the reference Reynolds number $\mathrm{Re}_0 = \rho_0 V_0 L_0/\mu$ (μ is the shear viscosity), the reference Prandtl number $\mathrm{Pr} = C_p \kappa/\mu$ (C_p is the specific heat at constant pressure and κ is the diffusion coefficient), and the reference Mach number $M_0 = V_0/c_0$ where $c_0 = \sqrt{\Gamma R T_0}$ is the typical sound speed and Γ is the ratio of the specific heats. The symbol $\delta_{i,j}$ is the Cronecker delta. This form of the Navier–Stokes equations is the same as that in *Miura and Kida* [1994], and in *Miura et al.* [2002, 2004]. In the inviscid and non–diffusive limit $\mu \to 0$ and $\kappa \to 0$, the system of equations (28)–(33) allows the Grad–Shafranov solution presented in the previous section.

In this section the equations (28)–(33) are solved numerically firstly for the dust devil problem with no–slip boundary condition at the bottom sand surface and with the free

boundary condition at the other boundaries. We approximately cut out the vortex solution at the center of the computational box of the dust devil simulation by the Oseen's vortex with an axial flow, embed the solution in the triply–periodic box and simulate its nonlinear evolution by the use of a pseudo–spectral code, which has been used in *Miura* [2002,2004], in order to see the evolution more closely with higher numerical precision.

The numerical simulations have been carried out by the use of the MUlti Theoretical Subjects Utility/compressible Navier–Stokes 3D (MUTSU/cNS3D) code. This code is the Navier–Stokes–solver version of the MUTSU/MINOS (MINOS is for MHD In Non–Orthogonal System) code, which has been used for studies of MHD instability in nuclear fusion [*Miura and Nakajima*, 2010]. These codes are equipped with computation modules to approximate a partial difference either by the fourth–order finite difference scheme, the eighth–order compact finite difference scheme, or the Fourier–spectral method. In the MUTSU/cNS3D code, the compressible Navier–Stokes equations (28)–(33) are described in a fully conservative form and are applicable to generalized curvilinear coordinates, to rectilinear Cartesian coordinates or in uniform Cartesian coordinates. The applicability of the code to fluid instability has been verified in *Miura and Nakajima* [2010] through detailed comparison of simulation results to the linear eigenfunctions of fully three–dimensional instabilities. *Miura and Nakajima* [2010] show that strong poloidal motions can generate still stronger toroidal motions. In this dust devil work we choose uniform, orthogonal Cartesian coordinates in the three–dimensional space so that the metrics are all constant in the space. The essence of our simulations is two–fold: (1) we show that the swirling motions on a horizontal plane (toroidal flow) is generated autonomously due to the instability described in the previous sections, and (2) we observe how the sand

particles are transported in the simulations. Although dynamics of Burgers vortex have been studied extensively, autonomous generation of a swirling flow due to the instability of the axial (poloidal) flow in the context of Secs. 2 and 3 is not well studied. Also, the particle transport of the test particles in the Burgers vortex is not sufficiently studied in 3D. As we will see in the succeeding paragraph, numerical simulations with these boundary conditions which generate dust devil flows are a form of the Burgers vortex with complex axial flows. After we show the generation of the toroidal flow out of the poloidal flow due to the instability, we take out a central region of the dust devil–like flow and put in a triple–periodic condition so that the velocities can be resolved on a higher resolution grid. For simplicity in the second simulation, the temperature is uniform in the axial (z–direction).

3.2. Numerical simulations of dust devil generation by the unstable vertical convection

By the use of the MUTSU/cNS3D code, we first carry out a simulation similar to those in $Gu, et al.$ [2006] by solving Eqs. (28)–(33) for a rectangular box of $L_1 \times L_2 \times L_3 = 4\pi \times 4\pi \times 10\pi$. The principal difference from the analytic solutions shown in Sec. 3 is that the equations of the continuity, momenta and total energy are solved numerically with the viscosity and the heat conductivity, under the boundary condition for the dissipative flows. The no–slip condition with the initially–given temperature is imposed on the bottom (ground surface) plane. The absorbing condition with the constant pressure gradient which stabilizes the upward flow is imposed on the top plane, with gradually–increasing viscosity for $z > 5\pi$. The temperature on the bottom plane is taken as consistent with that in $Gu, et al.$ [2006]. In the initial condition, the flow is given by Eq. (22) with a

small–amplitude perturbation. We also allow that the upward velocity is below or above the Mach number 0.1.

In Fig. 3, the initial velocity vector is shown on (a) (x, z)–plane at $y = 0$, and in (b)–(d) on the (x, y)–plane at $z \simeq \pi/4, \pi/2, 2\pi$, respectively. Figure 3(a) shows how a column of upwelling air convergent in the core drives an increasing strong toroidal velocity increasing with height and decreasing with radius. Figure 3(b)–(d) shows that there are only converging/diverging flows at each horizontal plane and that the flow swirling on the planes is initially very weak. In Figs. 4 and 5, the velocity vectors on the same four planes at later times, $t = 3.8$ and $t = 4.8$, are shown. It is clear that the swirling motions on the horizontal plane is strongly enhanced in the course of the time evolution. In these figures we see the flow velocities increase from the base to the top of the structure. At sufficient height where the Brunt Väisällä frequency has become strong again the flow turns around and falls $v_z(r, z) < 0$ with gravity to form the poloidal part of circulation. Though several mechanisms for generating vertical vorticity in dust devils have been suggested [*Ito, et al.*, 2013], this is the first clear simulation of the mechanisms. Our simulations show clearly that the nonlinear phase of the buoyancy instability is transferring energy to the toroidal flow by the dynamics of the vertical–vorticity equation described in Sec. 3. In the terminology of atmospheric dynamics, the process is one in which the horizontal vorticity generated baroclinically where there is a downdraft or updraft region plays a critical role for generating vertical vorticity through the nonlinear couplings. The observations in Figs. 3–5 show the details of the process that gives rise to the exponential growth of the initial seed of horizontal rotation Ω. The figures also show that the fluid motions on the horizontal planes are not dominated by a single vortex anymore at $t = 4.8$. The nonlinear

dynamics moves to complex structures which consist of multiple vortices. The complexity of flow is studied more closely in the next subsection.

In Fig. 6, the time evolution of the poloidal and toroidal components of the vorticity squared, $\Omega_H = \langle \omega_r^2 \rangle + \langle \omega_\theta^2 \rangle$ and $\Omega_Z = \langle \omega_z^2 \rangle$ are shown. Here the brackets indicates the volume average $\langle \cdot \rangle = \int_0^\pi dr \int_0^{2\pi} d\theta \int_0^{H/4} dz$, where $x = r\cos(\theta)$ and $y = r\sin(\theta)$. Initially, Ω_H is much larger than Ω_Z because of the initial condition. In the initial transient phase of the simulation $t < 1$, the averaged horizontal vorticity Ω_H decreases. Then Ω_H increases because the vertical flow is enhanced by the buoyancy instability until the growth is saturated at $t = 3$. During the time evolution Ω_Z is enhanced. The enhancement of Ω_Z is essentially due the conversion of the vertical flow into the swirling motions on the horizontal plane while conserving energy.

3.3. Vortex core simulations for fine structures in dust devil

Next, we focus on the vortex deformation at the dust devil core. We trim the dust devil vortex solution at the center out of the computational box, approximately expressing the solution initially by the Oseen's vortex (the Burgers vortex without the shear) with an axial flow, and embed the solution in the triply–periodic box. Then the evolution of the vortex is simulated by the use of the pseudo–spectral code in order to see the evolution.

In Fig. 7 we show three frames from the pseudospectral computation. The initial axial flow is similar to that in Eq. (22) but initially uniform in the vertical direction. The simulation shows the core evolution of the dust devil with sand particles passively convected. The grains of sand shown as the dots in these three frames rise and fall with the flow of the neutral atmospheric gas [air]. These three frames in Fig. 7 show an intermittency in the development of the helical structure of the column. The left frame

[001] at early time has a weak helical modulation, the middle frame [150] shows a strong helical modulation and the right frame [223] at late time has again a smaller amplitude helical modulation. The time interval spans approximately four revolutions of the dust devil. The movies show that the structure fluctuates slowly in time as it rotates. Over the course of 4 rotations we see low mode number $m = 2, 3, 4$ corrugations develop and dissolve in the column. Here we give the first, middle and final time structures from the movie in Fig. 7 after several rotations and frame after several more rotations. The overall structure is stable for many rotations and these substructures of helical corrugations are found to come and go in time. We do not attempt to analyze this complex dynamics further in this work.

Thus, we see the complex nonlinear helical structure results from the combination of the negative buoyancy of the lower density hot air driven by the solar heating of the soil. Followed by the onset of the poloidal flow pattern. Once the poloidal flow velocity has significant energy then any seed perturbation in the symmetry of the flow results in the exponential growth and saturation of the rotation motion. This complex nonlinear structure is then robust and moves horizontally easily as small external sheared flows dictate. In the process the structure finds new low lying areas of heated air to drive the thermal convection engine for hundreds of rotations.

3.4. Electrically–charged dust particles and their dynamics

The physics of the tribocharging and an estimation of the charge on silica dust particles for particles between 1-100 μm is given in *Ireland* [2010]. The physical and electrical properties of the reference dust particles used in the simulation are given in Table 1. The

dominant mechanical drag force vector F_D acting on the dust particles of mass m is

$$\boldsymbol{F}_D(r) = -\left(\frac{\pi d^2 \rho}{8}\right) C_D |\boldsymbol{v}_R| \boldsymbol{v}_R, \tag{34}$$

where vector v_R denotes the relative velocity of the particle with respect to the fluid (air). The drag coefficient C_D varies with Reynolds number $\mathrm{Re} = \rho |v_R| d/\mu$ approximately as

$$C_D = 24 \left(\frac{1 + 0.15 \, \mathrm{Re}^{2/3}}{\mathrm{Re}}\right). \tag{35}$$

The forces on particles during tribocharging is an active area of research since the processes are poorly understood, but are used in a number of practical applications [*Ireland and Jameson*, 2013]. Ireland and Jameson give comparisons of the force formulas using data in cylindrical cyclone tribochargers.

For the dust, in addition to this collisional drag force, there are three forces from (1) the pressure gradient F_p over the diameter d of the dust particle, (2) the buoyancy force F_B, and (3) the drag from the accumulation (mass accretion) of mass F_m. We follow *Gu, et al.* [2006] and take these forces as

$$
\begin{aligned}
F_p &= -\left(\frac{\pi d^2}{4}\right) \nabla p \\
F_B &= \frac{\pi d^3 (\rho_p - \rho)}{6} g, \\
F_m &= \frac{\pi d^3 \rho}{12} \frac{du}{dt},
\end{aligned} \tag{36}
$$

where ρ_p is the mass density of the dust particle and ρ is the mass density of the air.

3.5. Hydrodynamics with test particles

The boundary conditions are that at $z = 0$ the fluid velocity is $\mathbf{v} = 0$ and the surface temperature profile is fixed as $T(r) = T_a + 0.4(R - r)$ with $T_a = 313 \, \mathrm{K}$ for example. The sides of the cylinder and the top have Neumann boundary conditions when $v_r(r = R) > 0$,

but when there is an inward boundary velocity $v_r(r = R) < 0$, the vortex solutions give the hourly condition. We compare the results with $v_t(r = R, z) = 0$ with driving tangential flow $v_t(r = R, z) = (2\,\mathrm{m/s})(1 - \exp(-z))$ as used by *Gu, et al.* [2010].

Gu, et al. [2010] compare their results with wind tunnel data from *Dong, et al.* [2002], who express their data in terms of the parameterization of sand transport flux $q(z)$ given by

$$q_n(z) = a \exp\left(-\frac{z}{b}\right). \tag{37}$$

Data from Gu's simulation use the flux parameters as $a = 0.01\,\mathrm{g/ms}$ and $b = 10 - 20\,\mathrm{cm}$ with a scan over grain sizes giving that grains of size 100-250μm are most effectively lifted.

We are currently performing simulations using the hydrodynamic and magnetohydrodynamic codes of *Miura and Nakajima* [2010], using the parameters given by *Gu, et al.* [2010]. From experience in Texas, we know that the dust storms in the panhandle and west Texas bring significant layers of dust even into homes in Austin and San Antonio. Dust storms can reduce visibility to 1 km [*Goudie*, 1983].

4. Proposed Laboratory Experiments

The ability to add dust emission models to the Global Circulation Models (GCMs] would be an important improvement for weather and climate modeling. To start this activity it would be important and cost saving to test or validate the model with laboratory experiments. Testing the model with atmosphere data would be difficult owing to the many uncontrolled variables. Thus, we describe in this section a possible validation experiment for the model. The proposed experiment is shown in Fig. 7. The atmosphere and dust

are to be contained in a glass cylinder of 0.75-1 m diameter and 1.5-2.0 m height. The cylinder will be closed at the bottom by a metallic electrode which will be temperature regulated. The desired temperature range will be from room temperature up to 400 K. The top of the cylinder will also be closed by a glass electrode with a conductive metallic layer which will be kept at room temperature. Each electrode will be independently biased ($V_{\text{bias}} \sim 0 - 5\,\text{kV}$) in order to study the influence of an electric field on the formation of dust devils. On the bottom electrode, a layer of calibrated dust particles will be spread (mono–sized particles or a mixture of small and large particles). The material and size of the dust particles as yet to be defined. The considered size range is 10-1000μm and the proposed materials are silica, melamine formaldehyde and polystyrene. Gas (dry air, nitrogen or argon) will be injected in the cylinder by a tube located a few centimeters above the particle layer and extracted from the system by another tube located below the top electrode. The pressure inside the cylinder will be controlled in the range 0.5-3 atm. Experiments in both flowing gas and static gas configurations will be performed.

In order to track the motion of the dust particles, a two–laser sheet illumination system will be installed. The first sheet will be horizontal and parallel to the lower electrode; its position will be adjustable. The dust particles will be imaged with a high–speed video camera placed above the transparent top electrode. The second laser sheet will be vertical and will be positioned to go through the cylinder axis. A second high–speed video camera will be used to record the particle motion from the side.

5. Conclusion

We derive the critical temperature gradient condition for the onset of a vertical and horizontal convection from solar heating of the surface soil. Above the critical temperature

gradient the internal gravity waves are unstable and grow exponentially in amplitude. The limit on the growth occurs when the nonlinear coupling of the driven poloidal flows, meaning the vertical and radial velocity components in the cylindrical model of the dust devil, become sufficient to drive the toroidal flows. The poloidal flow has toroidal vorticity vector which through the 3D equations for the vorticity drives a toroidal flow producing a vertical vorticity. In the core of the structure the vortex is modeled with the Burgers vortex that includes the viscosity of the air as the dissipation mechanism. A steady nonlinear state is reached provided the vortex structure moves over freshly heated desert soil to maintain the strength of the thermal instability in the vertical flow in the core of the dust devil. A small external shear flow may serve as finite amplitude "kick" or perturbation to start the nonlinear rotation dynamics and determine the direction of rotation. In the field reports an approximately symmetric distribution of cyclonic and anti–cyclonic dust devils are recorded. The 3D nonlinear simulations are shown to verify this sequence of steps and allows one to visualize in detail with movies and with cross–sectional plots of the velocity vector flow fields both in the growing phase and the quasi–stationary nonlinear saturated states of the dust devil. The results show that there is a variety of nonlinear states available depending on the geometry and the parameters. However, the states found resemble well those reported in the field data summarized here. Thus, the simulation code may be useful for building models for the source rate of injecting dust into the atmosphere for global weather predictions for sub grid–scale sources of dust in general circulations models.

Here we report new simulations with 3D codes for the complex nonlinear dynamics of the dust devil that evolves when the near–surface air has a sufficient temperature gradient.

We derive the critical temperature gradient for the onset of the initial vertical convection that evolves from the buoyancy instability when the hot air near the sandy surface becomes lighter than the heavier cooler overlying air. Then we show that once there is sufficient amplitude or energy in the vertical convective cells or poloidal flows there is the onset of a toroidal rotational instability of the nonlinear parametric instability type from nonlinear interactions in this complex system. For a simple model of the poloidal convection we derive the formula for the growth rate of the toroidal rotation.

The structure is mathematically analogous to the tokamak configuration where the divergence free vector is the helical magnetic field with this vector field is the corresponding current density derived from the curl of the magnetic field from Ampere's law. Tokamak also has show a spontaneous symmetry breaking when heated sufficiently, past a critical external power, with the onset of fast toroidal flows [*Greenwald, et al.*, 1995].

References

Arnas, C., A. Michau, G. Lombardi, L. Couedel, and Kishor Kumar K, Effects of the growth and the charge of carbon nanoparticles on direct current discharges, *Phys. Plasmas, 20*, 013705 (2013), `http://dx.doi.org/10.1063/1.4776681`.

Balme, M., and R. Greeley, Dust devils on Earth and Mars, *Geophys. Rev., 44*, 3 (2006), `http://dx.doi.org/10.1029/2005RG000188`.

Chu, D. A., Y. J. Kaufman, C. Ichoku, L. A. Remer, D. Tanré, and B. N Holben, Validation of MODIS aerosol optical depth retrieval over land, *Geophys. Res. Lett., 29*, 12, MOD2–1–MOD2–4 (2002), `http://dx.doi.org/10.1029/2001GL01320`.

Crozier, W. D., Dust Devil Properties, *J. Geophys. Res., 75*, 24, 4583–4585 (1970), `http://dx.doi.org/10.1029/JC075i024p04583`.

DeMott, P. J., K. Sassen, M. R. Poellot, D. Baumgardner, D. C. Rogers, S. D. Brooks, A. J. Prenni, and S. M. Kreidenweis, African dust aerosols as atmospheric ice nuclei, *Geophys. Res. Letts., 30*, 14 (2003), `http://dx.doi.org/10.1029/2003GL01741.0`.

Dong, Z., X. Liu, H. Wang, A. Zhao, and X. Wang, The flux profile of a blowing sand cloud: A wind tunnel investigation, *Geomorphology, 49*, 219–230 (2002).

Farrell, W. M., *et al.*, Electric and magnetic signatures of dust devils from the 2000D2001 MATADOR desert tests, J. *Geophys. Res., 109*, E03004 (2004), `http://dx.doi.org/10.1029/2003JE002088`.

Farrell, W. M., P. H. Smith, G. T. Delory, G. B. Hillard, J. R. Marshall, D. Catling, M. Hecht, D. M. Tratt, N. Renno, M. D. Desch, S. A. Cummer, J. G. Houser, and B. Johnson, Electric and magnetic signatures of dust devils from the 2000–2001 MATADOR desert tests, *J. Geophys. Res.: Planets (1991–2012), 109*, E3, `http://dx.doi.org/10.1029/2003JE002088`.

Freier, G. D., The electric field of a large dust devil, *J. Geophys. Res., 65*, 10, 3504 (1960), `http://dx.doi.org/10.1029/JZ065i010p03504`.

Goudie, A. S., Dust storms in space and time, *Prog. Phy. Geog., 7*, 4, 502–530 (1983), `http://dx.doi.org/10.1177/030913338300700402`.

Greeley, R., *et al.*, Martian variable features: New insights from the Mars Express Orbiter and the Mars Exploration Rover Spirit, *J. Geophys. Res., 110*, E06002, `http://dx.doi.org/10.1029/2005JE002403`.

Greenwald, M., Boivin, R. L., Bonoli, P., Christensen, C., Fiore, C., Garnier, D., Goetz, J., Golovato, S., Graf, M., Granetz, R., Horne, S., Hsu, T., Hubbard, A., Hutchinson, I., Irby, J., Kurz, C., LaBombard, B., Lipschultz, B., Luke, T., Marmar, E., McCracken, G., Niemczewski, A., O'Shea, P., Porkolab, M., Rice, J., Reardon, J., Schachter, J., Snipes, J., Stek, P., Takase, Y., Terry, J., Umansky, M., Watterson, R., Wolfe, S., Bombarda, F., May, M., and Welch, B., *Phys. Plasmas, 2*, 2308 (1995), `http://dx.doi.org/10.1063/1.871254`.

Gu, Z., W. Wei, and Y. Zhao, An overview of surface conditions in numerical simulation of dust devils and the consequent near–surface air flow fields, *J. Atmospheric Sci., 63*, 1630 (2006).

Horton, W., *Turbulent Transport in Magnetized Plasmas*, Chps. 13 & 17, pp. 308–335 & 443–446 (2012), ISBN:978-981-4383-53-0.

Houser, P., *et al.*, *J. Geophys. Res.* (2003).

Ireland, P. M., Triboelectrification of particulate flows on surfaces: Part I – Experiments, *Technology, 198*, 2, 189–198 (2010), `http://dx.doi.org/10.1016/j.powtec.2009.11.017`.

Ireland, P. M., Triboelectrification of particulate flows on surfaces: Part II – Mechanisms and models, *Powder Technology, 198*, 2, 199–210, (2010), `http://dx.doi.org/10.1016/j.powtec.2009.11.008`.

Ireland, P. M., and G. J. Jameson, Particle dynamics in cyclone tribochargers, *J. Electrostatics, 71*, 449–455 (2013).

Ito, J., H. Niino, and T. M. Nakanishi, "Mechanism of Generating Vertical Vorticity in Dust Devils," private communication from Junshi Ito, Ocean Research Institute,

(Tokyo, Japan, 2013).

Kahn, R. A., B. J. Gaitley, J. V. Martonchik, D. J. Diner, K. A. Crean, and B. Holben, Multiangle Imaging Spectroradiometer (MISR) global aerosol optical depth validation based on two years of coincident Aerosol Robotic Network (AERONET) observations, *J. Geophys. Res.: Atmospheres (1984–2012), 110*, D10 (2005).

Kida, S. and H. Miura, Identification and analysis of vortical structures, *Eur. J. Mech. B/Fluids, 17*, 471-488 (1998).

Kok, J. F. and N. O. Renno, Enhancement of the emission of mineral dust aerosols by electric forces, *Geophys. Rev. Lett., 33*, 19 (2006), `http://dx.doi.org/10.1029/2006GL026284`.

Lacks, D. J., and A. Levandowsky, Effect of particle size distribution on the polarity of triboelectric charging in granular insulator systems, *J. Electrostatics, 65*, 107–112 (2007), `http://dx.doi.org/10:1016/j.elsat.2006.07.010`.

Li, X., Huw Morgan, Drew Leonard, *et al.*, *Astrophys. J. Lett., 752*, 2 (2012).

Miller, R. L., R. V. Cakmur, J. Perlwitz, V. Geogdzhayev, P. Ginoux, D. Koch, K. E. Kohfeld, C. Prigent. Mineral dust aerosols in the NASA Goddard Institute for Space Sciences Model E atmospheric general circulation Model E, *J. Geophys. Res., 111*, D06208 (2006), `http://dx.doi.org/10.1029/2005JD005796`.

Mishchenko, M. I., *et al.*, Modeling phase functions for dust–like tropospheric aerosols using a shape mixture of randomly oriented poly–disperse spheroids, *J. Geophys. Res., 102*, 16,831–16,847 (1997).

Miura, H. and N. Nakajima, *Nucl. Fusion, 50*, 054006 (2010), `http://dx.doi.org/10.1088/0029--5515/50/5/054006`.

Miura, H., Excitations of vortex waves in weakly compressible isotropic turbulence, *J. Turbulence, 5*, 010 (2004).

Miura, H., Analysis of vortex structures in compressible isotropic turbulence, *Comp. Phys. Commun., 147*, 552–555 (2002) .

Miura, H. and S. Kida, Vorticity generation by shock-vorticity interaction, *J. Phys. Soc. Jpn., 63*, 4000–4010, (1994), `http://dx.doi.org/10.1143/JPSJ.63.4000`.

Oke, A. M. C., Tapper, N. J., Dunkerley, D. Willy-willies in the Australian landscape: The role of key meteorological variables and surface conditions in defining frequency and spatial characteristics, *J. Arid Environ., 71*, 201-215 (2007).

Onishchenko, O. G., Pokhotelov, O., Horton, W., Smolyakov, A., Kaladze, T., and Fedun, V., Rolls of the internal gravity waves in the Earth's atmosphere, *Ann. Geophys., 32*, 181-186 (2014), `http://dx.doi.org/10.5194/angeo-32-181-2014`.

Renno, N. O., M. L. Burkett, and M. P. Larkin, A simple thermodynamical theory for dust devils, *J. Atmos. Sci., 55*, 3244–3252 (1998), `http://dx.doi.org/10.1175/1520--0469(1998)055<3244:ASTTFD>2.0.CO;2`.

Renno, N. O., V. J. Abreu, J. Koch, P. H. Smith, O. K. Hartogensis, H. A. R. De Bruin, D. Burose, G. T. Delory, W. M. Farrell, C. J. Watts, J. Garatuza, M. Parker, and A. Carswsell, MATADOR 2002: A pilot field experiment on convective plumes and dust devils, *J. Geophys. Res., 109*, 2156-2202 (2004), `http://dx.doi.org/10.1029/2003JE002219`.

Schmidt, D. S., R. A. Schmidt, and J. D. Dent, *Electrostatic Force on Saltating Sand, 103*, D8, 8997–9001 (1998), `http://dx.doi.org/10.1029/98JD00278`.

Schwarzschild, K., Gesammelte Werke: Collected Works (Springer Verlag, 1998).

Twomey, S., Pollution and planetary albedo, *Atmos. Environ., 8*, 1251–1256 (1974).

Wedemeyer–Böhm, S., E. Scullion, O. Steiner, *et al., Nature, 486*, 505 (2012).

Wedemeyer–Böhm, S., and L. Rouppe van der Voort, Small–scale swirl events in the quiet Sun chromosphere, *Astron. Astrophys., 507*, L9–L12 (2009).

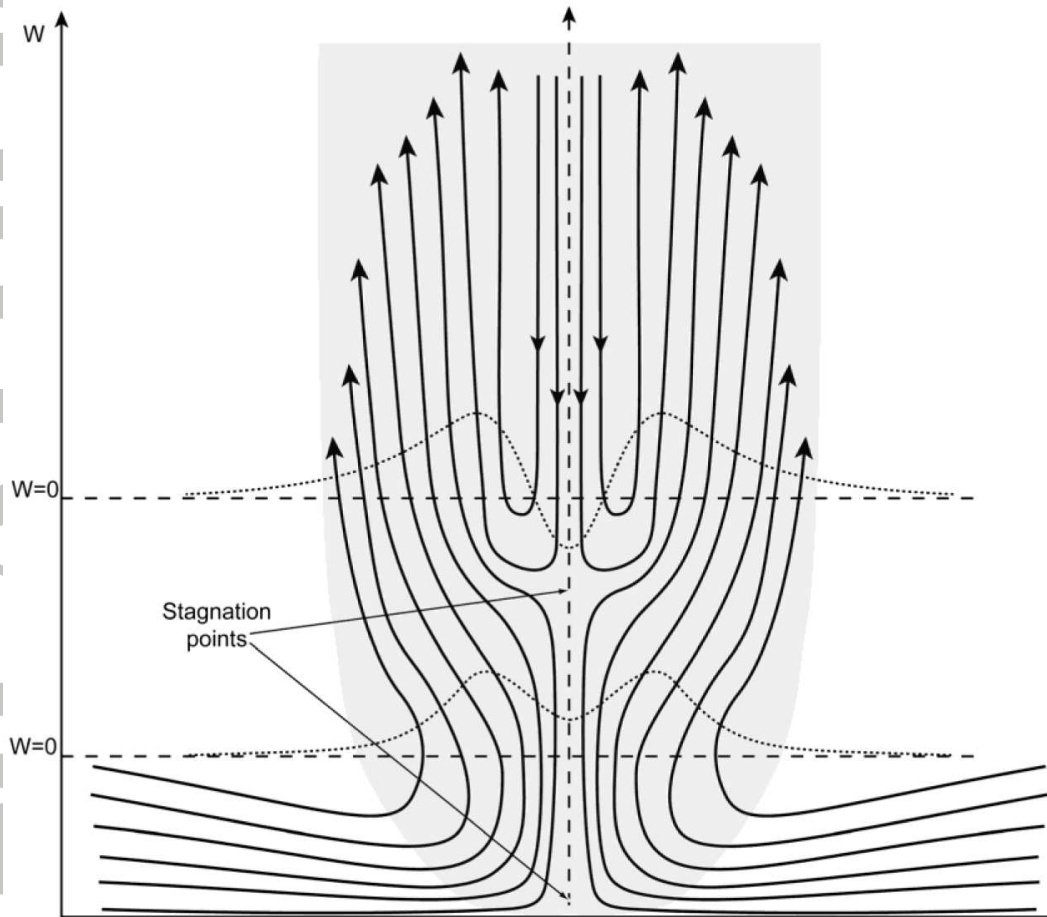Zhang, H., X-J. Zheng, and T. Bo, Electrification of saltating particles in wind-blown sand: Experiment and theory, *J. Geophys. Res., 118*, 21, 12,086–12,093 (2003), `http://dx.doi.org/10.1002/2013JD020239`.

Figure 1. Top figure (a) is a schematic diagram of the vertical flow with two stagnation points given by *Balme and Greeley* [2006] who based the diagram on observations that sometimes show a downward–flow core velocity in the dust devil above a certain height. They note that this downward flow may not be present in all cases and is only measured in certain cases. The lower figure (b) shows the gravitation force and the electric polarization $\vec{P}$ in the dust devil created by the triboelectric charging of the dust grains. The negatively charged grains are supported against gravity and the pull of the positive charges by the friction with up going air mass.
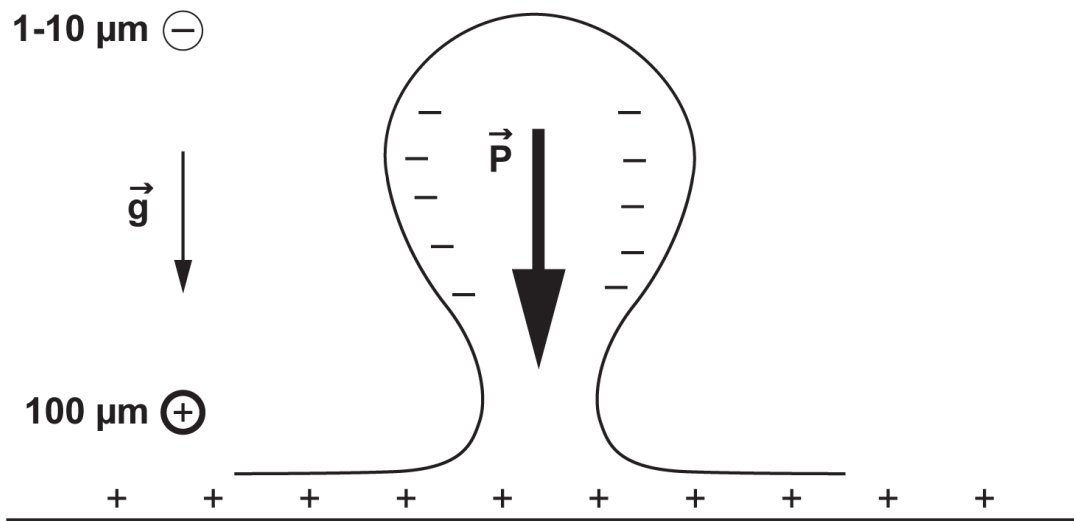
Figure 2. Diagram of the basic mechanism of the temperature gradient driven incompressible vertical toroidal vortex structure for the dust devil. The saltation in the sand layer is indicated schematically and the triboelectric charging from the collisions between the small $\sim< 20\mu$ m particles with the large 100μ m sand particles produces the electric dipole moment in the structure. The small, light negatively charged particles rise to the top of the structure $z = H$.
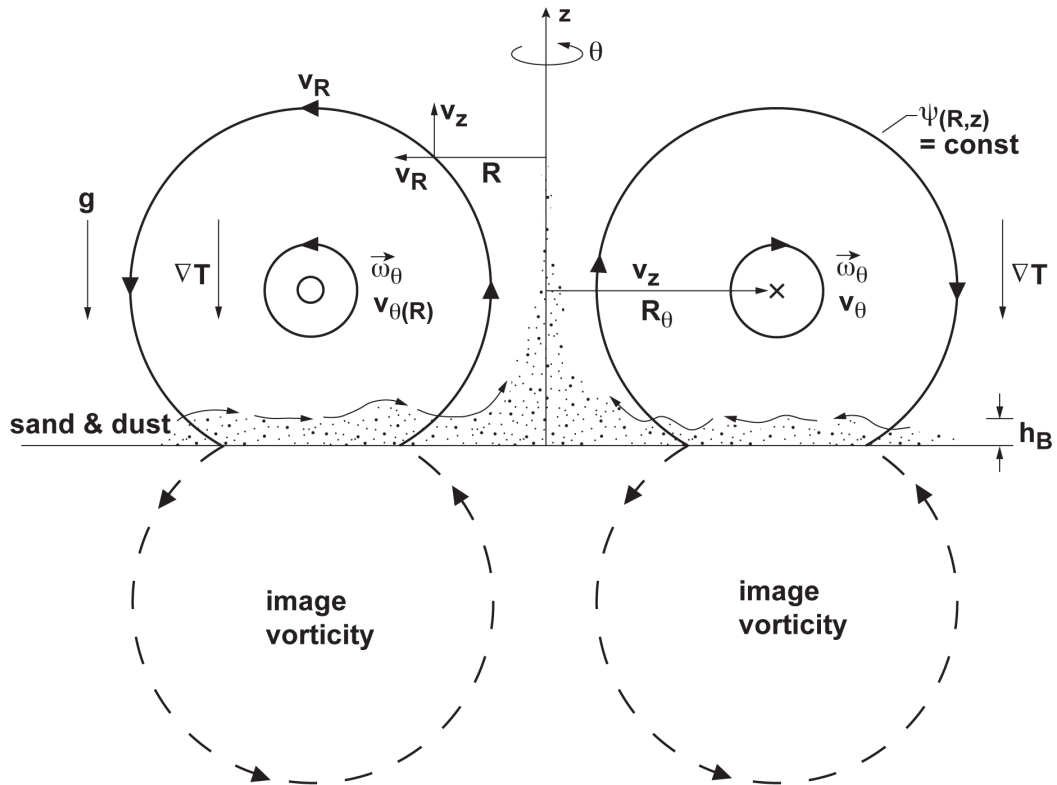
Figure 3. Initial flow at $t = 0$ in the simulation box of $2\pi \times 2\pi \times 10\pi$, on (a) (x, z)–plane at $y = 0$, and (b)–(d) on (x, y)–plane at $z \simeq \pi/3, \pi/2, 2\pi$, respectively.
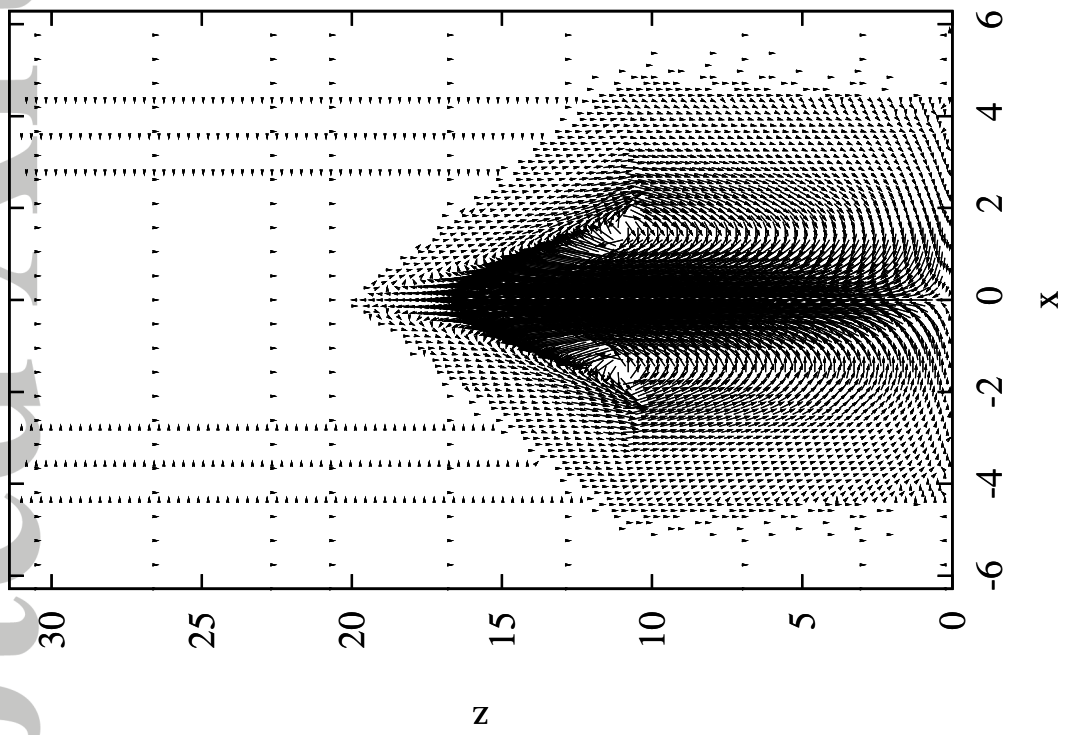
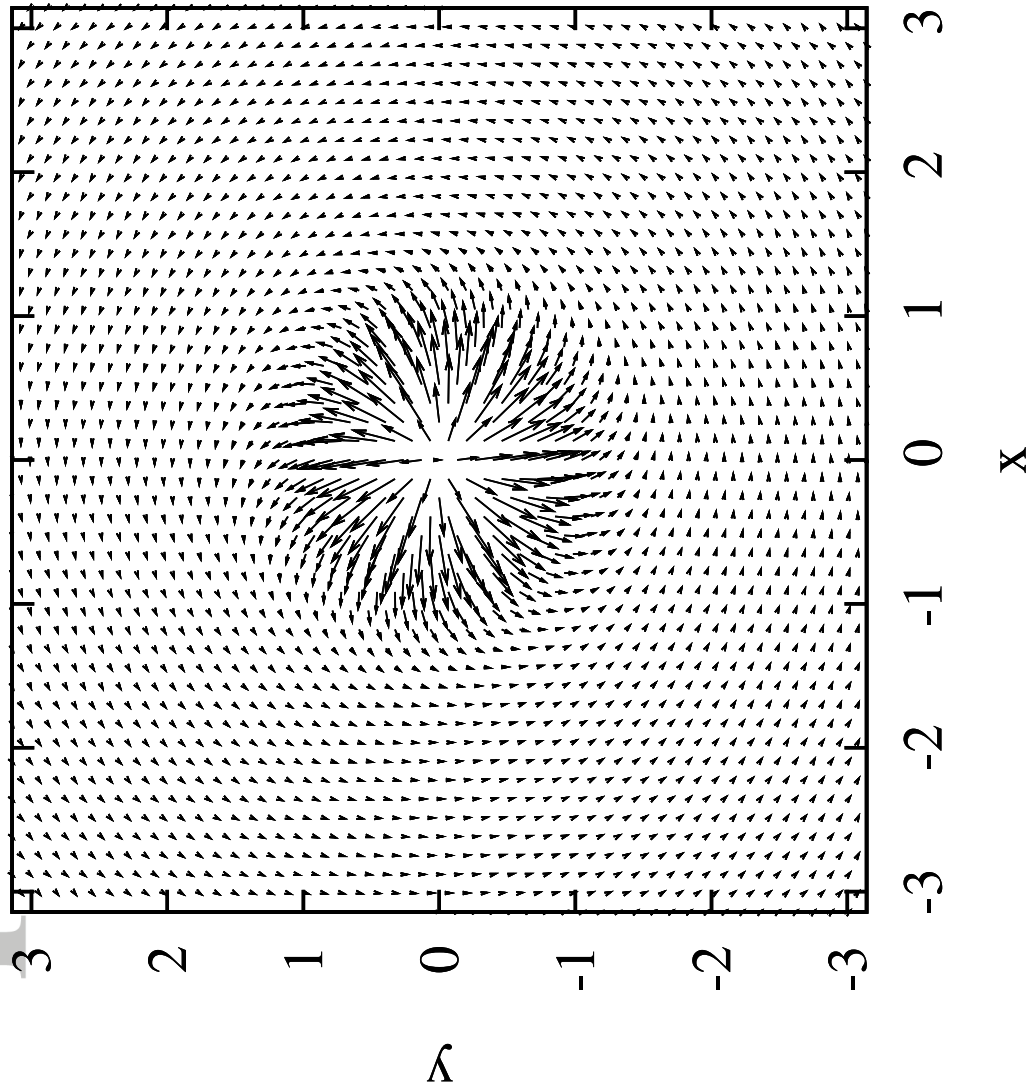**Figure 4.** Velocity vector plots at $t = 3.8$, on the same planes (a)–(d) as those in Fig. 3.

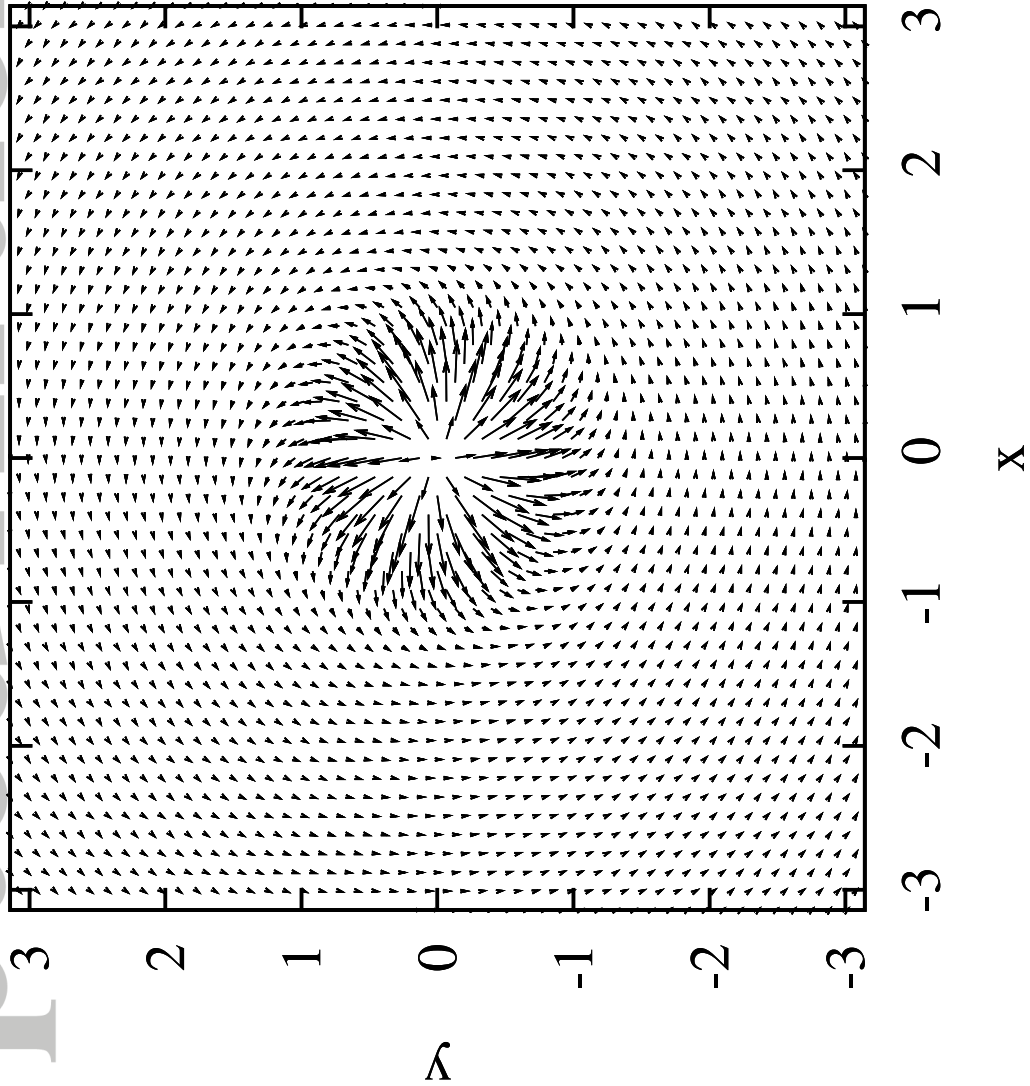**Figure 5.** Velocity vector plots at $t = 4.8$, on the same planes (a)–(d) as those in Fig. 3.

Figure 6. Time evolution of the poloidal and toroidal components of the vorticity squared, $\langle \omega_r^2 \rangle + \langle \omega_\theta^2 \rangle$ and $\langle \omega_z^2 \rangle$ In the period from $t = \approx 1.0$ to 4.5 the exponential growth of the vertical vorticity derived in Sec. 3 appears and then saturates. In this saturated complex state nonlinear helical substructures emerge as shown in Fig. 7.
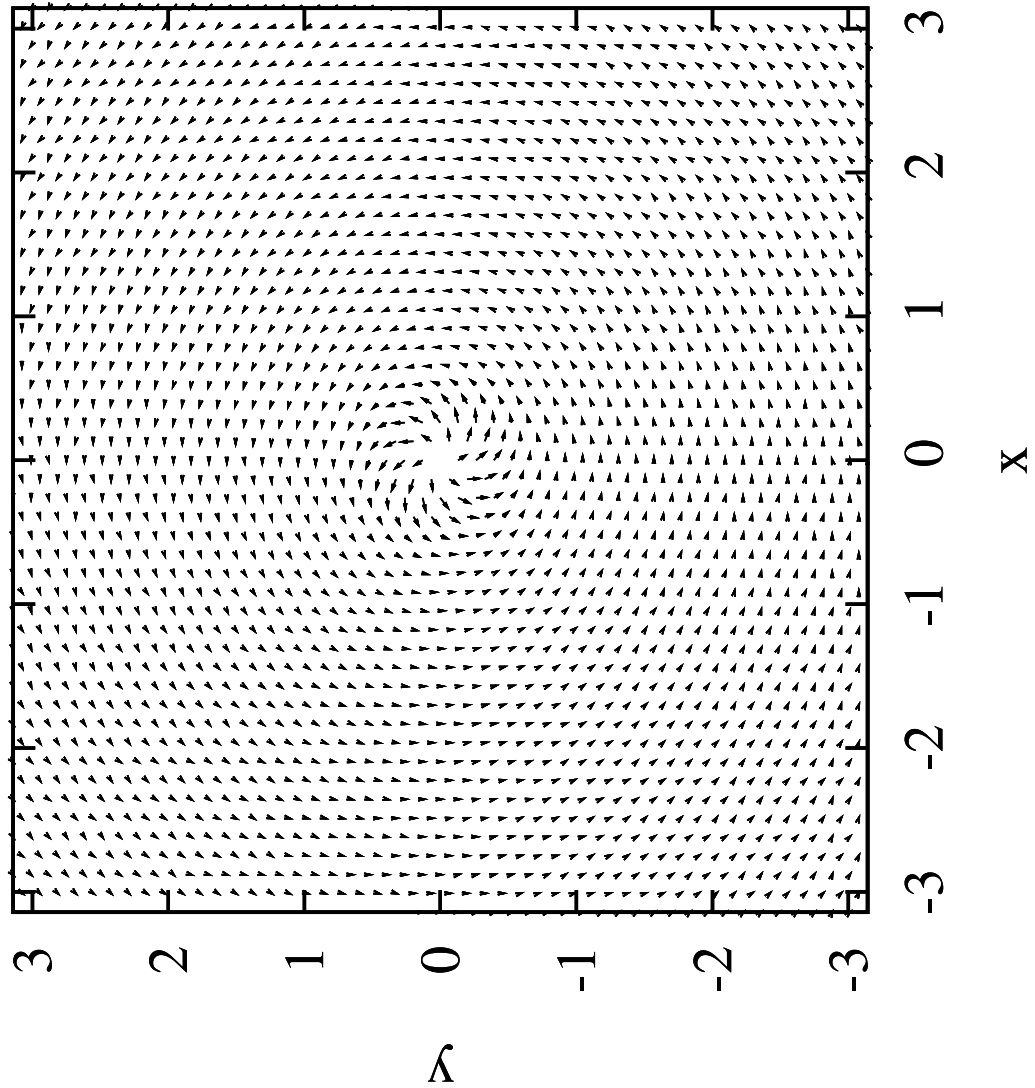
Figure 7. Three frames from a nonlinear run with test particles in the mid–altitude height of the dust devil simulation. The movie shows the formation of a deep, smaller–scale helical formation in the initial column [001] shown in the left frame going to the middle frame [150] and subsequently the decay of the deep helical modulation to a more symmetric central column in going from the middle frame to a later time frame in the right frame [237]. Thus the nonlinear dynamics has several frequencies forming a weakly chaotic time dependence of the structure [Horton, Chaos and Structures, Ch. 4].
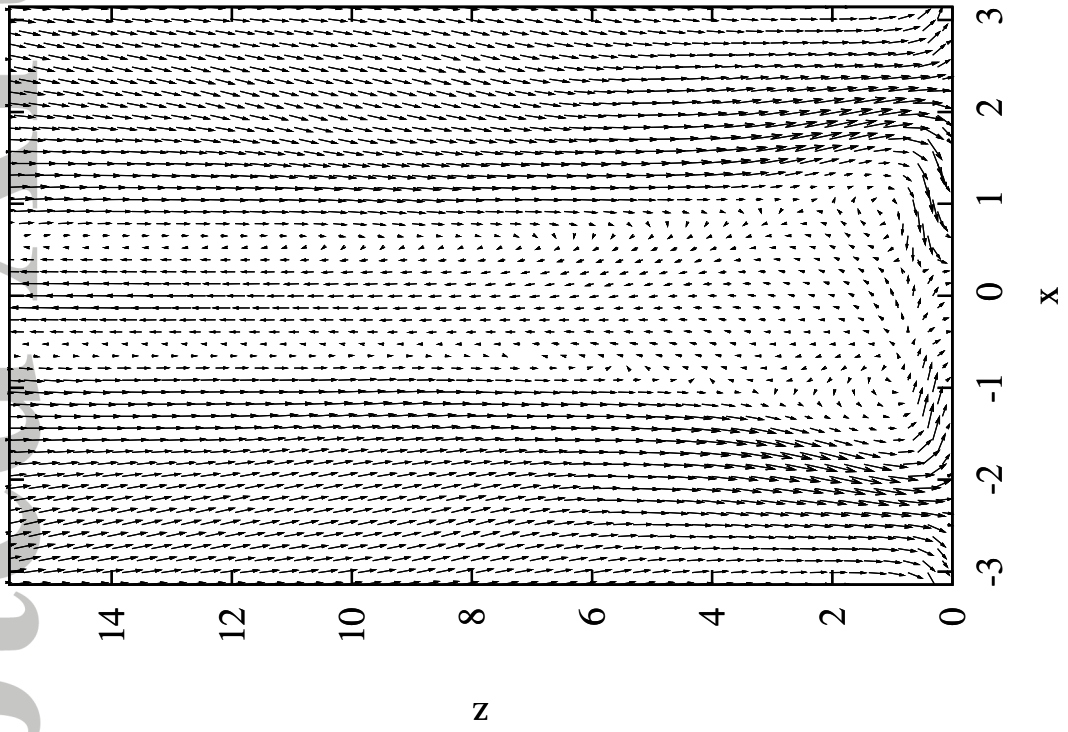
Figure 8. Schematic of the proposed experiment

Table 1. Properties of quartz and sand dust particles

	$1\mu\,$m	$100\mu\,$m
Dust particle radius Quartz sand mass density $\rho_m = 3\,\text{g/cm}^3$		
Capacitance $C_d = 4\pi\epsilon_0 r_d$	$C_d = 10^{-16}\text{F}$	$C_d = 10^{-14}\text{F}$
Charge on grain for potential of 10 V and number N_e of electrons	$Q_d = 10^{-15}C \rightarrow$ $N_e = 10^4$	$Q_d = 10^{-12}C \rightarrow$ $N_e = 10^6$
Mass of grains and number of SiO$_2$ molecules in grain	$M_d = 3 \times 10^{-12}$g $N_{\text{SiO}_2} = M_d/6$ amu $= 5 \times 10^{10}$	$M_d = 3 \times 10^{-6}$g $N_{\text{SiO}_2} = M_d/60$ amu $= 5 \times 10^{16}$
Mass $M_a =$ of air molecules [70% N_2 + 30%] O$_2$	$M_a = 4.2 \times 10^{-23}$	$M_a = 4.2$ $\times 10^{-23}$g
Charge in volume $H_d = 10\,$m by $R_d = 10\,$m volume $V_d = 10^3\,\text{m}^3$ of dust for density $n_d = 10^6/\text{cm}^3$	$Q = 10^{-15}C/$ grain $\times 10^{11}$ grains $= 1.1 \times 10^{-4}C$	Dust density for 10^{11} grains in volume $= 10^3\,\text{m}^3$ is 1.6×10^8 grains/m^3 = 160 grains per cc
Potential drop to ground from $H_d = 100\,$m	$V = 9 \times 10^9\,Q/$ $H_d = 9\,$kV	$V = 900\,$kV
Electric field from ground to center of the charge cloud	$E = V/h_d = 1\,$kV/m	$E = 100\,$kV/m

Table 2. Parameter of the proposed experiments

Cylinder height	1.5-2.0 m
Cylinder diameter	0.75-1 m
lower electrode	metal
top electrode	conductive glass
lower electrode temperature range	300-400 K
upper electrode temperature	300 K
Electrode bias	0-1 kV
Particle size	10-1000 μm
Diagnostics	laser sheet and high speed video camera